3

Tera50+ – sub-mm-wave 100 Gbit/s Fiber-Wireless Transmission System

Matthias Steeg, Jonas Tebart, Sebastian Dülme, Andreas Stöhr

ZHO/Optoelectronics, University of Duisburg-Essen

Florian Exner, Andreas Czylwik

Communication Systems, University of Duisburg-Essen

Mai Alissa, Thomas Kaiser

Digital Signal Processing, University of Duisburg-Essen

CONTENTS

DOI: 10.26127/BTUOpen-5909

3.1 Introduction

As the exponential growth of global IP traffic continues, mobile devices occupy an increasingly larger portion with a share above 70% expected by 2022 [109]. Especially (ultra) high definition video services consumed on tablets and smartphones are causing this shift, which exemplifies the change of network usage in modern societies, where mostly wireless and mobile services are used – even indoors. This ever increasing demand for high speed broadband services drives the research of new technologies for wireless communications. The upcoming 5G next generation of mobile communication addresses these trends and promises a 1000-fold increase in network capacity and > 10 Gbit/s data rate transmission per small cell through advances in spectral efficiency, cell size reduction and larger bandwidths [110].

In order to support a vastly increased number of high capacity cells, the backhaul throughput has to be enhanced significantly. So optical fiber transport is vital to provide 5G mobile access with its vast bandwidth and throughput capabilities. Due to the elaborate process of laying fiber in densely populated or building obstructed locations, timely and cost-effective 5G roll-out will complement fiber routes with high bandwidth fixed wireless backhauling links. Since high bandwidth mm-wave frequency bands are already projected for 5G access, sub-mm-wave and THz bands are also envisaged for backhauling as they provide substantially larger bandwidths such as 50 GHz in the 300 GHz J-band [111].

With regards to the steep latency and data rate requirements, fiber-wireless convergence is a key topic in 5G and thus analog Radio-over-Fiber transport already attracts interest for backhauling as well as access networks [112, 113]. In addition to 5G backhauling, fiber-wireless transmission systems in the sub-mm-wave and THz bands are promising candidates for > 100 Gbit/s mobile access beyond 5G.

In the Tera50+ project we have focussed on photonic wireless transmission systems, which are scalable in frequency from microwave over (sub-)mm-wave to THz bands. Thereby, the baseband part can be highly digitized and remains the same, when scaling the radio frequency via photonic techniques. In particular, Tera50+ showcases the application of two bands in the mm-wave and THz region, that offer 14 GHz bandwidth around 60 GHz and 50 GHz bandwidth around 300 GHz.

In the following, the utilized coherent Radio-over-Fiber mm-wave and THz transmission system with envelope detection is outlined. After that the analytically developed and experimentally proven channel models for the 60 GHz and 300 GHz bands are presented. Finally, the application of the fiber-wireless transmission system for high bandwidth OFDM measurements is demon-

strated in experiments achieving > 100 Gbit/s data rates, before the chapter is concluded.

3.2 Coherent Radio-over-Fiber THz Transmission System

Optical fiber transport is essential for wireless networks to provide low-loss and vast bandwidth for signal distribution. Modern fiber-wireless networks employ (digitized) Radio-over-Fiber (RoF) as transparent transport for fronthauling wireless signals to the radio access units [112, 114]. For > 100 Gbit/s wireless transmission at sub-mm-wave carrier frequencies traditional RoF systems would require unfeasible optical modulator bandwidths to directly generate the optical RF signals. In contrast, optical fiber links with complex baseband modulation for data rates in excess of 100 Gbit/s are already available.

Therefore, a coherent Radio-over-Fiber scheme is employed, where the data signals are modulated onto the optical carrier and another optical tone is used as a local oscillator. Then, the photodetector at the RAU generates the RF data signal through heterodyne detection of the modulated optical data signal and the optical LO. The radio frequency is given by the beat frequency of the optical carrier and LO. As lasers are available covering a wide range of frequencies, the main limitation to the range of possible radio frequencies generated this way is the speed of the opto-electronic conversion [111].

Generating THz signals in this fashion has major advantages over electrical generation. As electrical oscillators usually employ large multiplier chains to generate the desired radio frequency from a low starting frequency phase-noise is a major issue in those systems [115]. In comparison, photonic RF carrier generation can achieve superior performance, when the carrier frequency offset is limited [116].

Another challenge is the availability of power amplifiers in the THz region. The generation of high power THz signals is impeded by the availability of high power amplifiers in this frequency range.

The issue of THz oscillators also affects the design of the receiver. Heterodyne detection requires an LO at the wireless receiver for down-conversion, which should be tunable to select from multiple channels transmitted over large bands. The aforementioned electronic LOs based on multiplier chains exhibit not only large phase noise, but also high power consumption, which prevents their usefulness for many applications especially as wireless receivers e.g. in mobile devices.

In this project Schottky-barrier detectors are employed at the wireless receiver, as we consider them best suited for fiber-wireless data transmission in the sub-mm-wave and THz bands. At these frequencies, electrical LOs for heterodyne detection lead to an upper limit in achievable spectral efficiency

and thus data rate for state-of-the-art purely electronic systems due to their fundamentally large phase noise [117].

Stable, low-noise fundamental oscillators are not yet available with suitable performance, so that the only alternative providing better phase noise is using optical frequency combs (OFCs). While optoelectronic oscillators (OEOs) with OFCs deliver record figures for phase noise, they are still bulky and not suitable for a small wireless receiver with mobility [118].

Using envelope detection circumvents these issues, as the stable IF carrier is supplied by the same baseband electronics as the modulated data signal, which leads to phase noise cancellation at the SBD, making it phase-noise insensitive [119].

The fact that no LO is required at the wireless receiver causes further benefits for the simple receiver architecture such as a reduced power consumption and no tuning requirements for changing frequency channels.

Similar to the photodiode, which converts the optical IF/baseband signal to RF by means of an optical LO fed through the same input, the Schottky-barrier diode (SBD) converts the received RF signal back to the modulated IF. Therefore, an IF carrier, which is added with the optical data modulation, is utilized for self-mixing down-conversion by the envelope detector.

After down-conversion subsequent digitization via a sampling oscilloscope is employed. The oscilloscope prevents the necessity for additional I/Q baseband circuitry and allows flexibility for optimizing the setup through experiments. Since it provides a large input bandwidth in excess of 60 GHz, it supports utilizing digital envelope detection for comparison to the SBD performance.

3.2.1 Transmission System Architecture

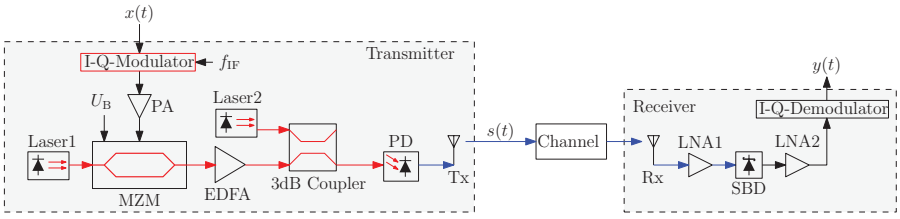

Figure 3.1
Basic Radio-over-Fiber THz Transmission system

We consider a transmission system as shown in Fig. 3.1 consisting of a Radio-over-Fiber transmitter and a coherent detection receiver. The transmitter uses two free running lasers and a Mach-Zehnder-modulator (MZM) to generate the transmit signal $s(t)$ at radio frequency from a complex-valued input signal $x(t)$. In the first step, the input signal $x(t)$ is I-Q-modulated onto

an intermediate frequency f_{IF}. The resulting real-valued signal is then amplified using a power amplifier (PA) in order to drive the electrical input port of a Mach-Zehnder-modulator.

The Mach-Zehnder-modulator modulates the electrical input signal onto the optical signal carrier provided by a laser diode (Laser1). Passing the optical carrier through the Mach-Zehnder-modulator causes power loss due to the optical insertion loss of the device. Additional power is lost in the Mach-Zehnder-modulator based on the chosen bias voltage U_{B}.

An Erbium-doped-fiber amplifier (EDFA) is used to compensate the losses of the MZM. It further boosts the optical power to yield a large RF signal from the photodiode (PD) together with a second carrier acting as optical local oscillator (Laser2). Therefore, the amplified optical signal and the second optical carrier are combined in a 3 dB-coupler and fed into a photodiode for heterodyne detection.

In order to achieve the highest power of the intended transmit signal $s(t)$ both the modulated carrier signal and the second optical carrier signal should be comparable in power when entering the photodiode. Then again the heterodyne detection offers the possibility to increase the generated RF power by means of a strong local oscillator (LO) in case the optical signal power is weak.

As the output power of the photodiode is up to $-11.0\,\mathrm{dBm}$ at 300 GHz no additional amplifier is needed before transmission. The RF signal generated by the PD is then radiated by a standard gain horn antenna (Tx). After wireless transmission over 1 m in the 60 GHz band and 20 cm in the 300 GHz band the signal is received by another horn antenna (Rx).

Since the transmitting and receiving antenna are highly directional with a gain of 23 dBi and 25 dBi of the WR15 and WR3 antennas, respectively, we assume line-of-sight (LoS) conditions for the channel. Thus, even slight misalignment of the horn antennas results in a substantial drop in received power, as observed during the measurements.

Before the received signal is detected by the SBD envelope detector, amplification is carried out using a low-noise amplifier (LNA1). Afterwards, the signal is amplified again (LNA2) at baseband and received by the oscilloscope. The digital sampling oscilloscope (DSO) supplies the digital I-Q-demodulator, which provides the output signal $y(t)$ of the transmission system.

3.2.1.1 Mach-Zehnder Modulator

In a Mach-Zehnder-modulator the optical input signal is split into two paths by a 3 dB-coupler as shown in Fig. 3.2. The phases of both paths are then modulated in opposite direction based on the electric input signal $x(t)$ to generate a phase difference between the two paths. By combining them again the output signal of the MZM is created.

Amplitude modulation of the optical carrier $E_{\mathrm{out}}(t)$ at the output of the Mach-Zehnder-modulator is realized due to the positive and negative interference of these phase modulated paths. The optical output signal $E_{\mathrm{out}}(t)$ of a

Mach-Zehnder modulator can be modeled as

$$E_{\text{out}}(t) = k_{\text{T}} E_{\text{in}}(t) \cos\left(\frac{\pi}{2U_\pi}\left(x(t) + U_{\text{B}} - U_{\text{max}}\right)\right). \tag{3.1}$$

In this model, k_{T} is the optical transmission coefficient of the Mach-Zehnder-modulator, U_{max} gives the position of the maximum transmission point, U_{B} denotes the applied bias voltage, U_π is the voltage difference between maximum-transmission point and minimum-transmission point U_{min} and $E_{\text{in}}(t)$ represents the optical input signal.

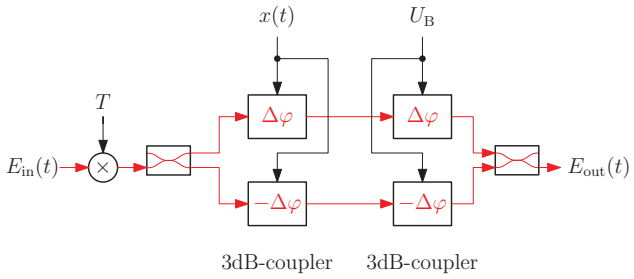

Figure 3.2
Block-diagram of a Mach-Zehnder-modulator

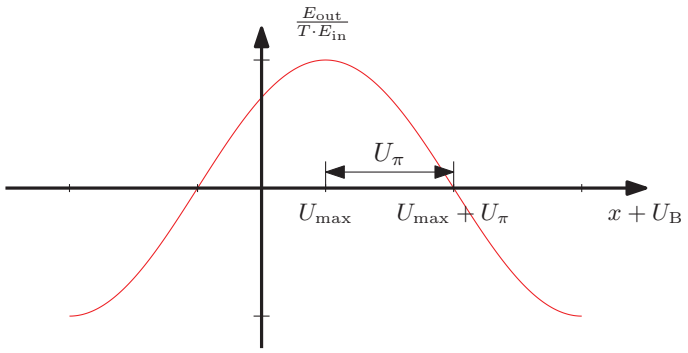

Figure 3.3
Input-output characteristics of the Mach-Zehnder-modulator

As can be seen from Fig. 3.3 the bias voltage affects the linearity of the operating region as well as a constant offset which corresponds to the optical carrier. Alternatively, the Taylor-series expansion of eq. 3.1 around the normalized, effective bias voltage $U_{\text{B,norm}}$ with

$$U_{\text{B,norm}} = \frac{\pi(U_{\text{B}} - U_{\text{max}})}{2U_\pi} \tag{3.2}$$

given by

$$E_{\text{out}}(t) = k_{\text{T}} E_{\text{in}}(t) \left(c_0 + c_1 \frac{\pi}{2U_\pi} x(t) + \sum_{i=2}^{\infty} c_i \left(\frac{\pi}{2U_\pi} x(t) \right)^i \right) \tag{3.3}$$

with

$$c_i = \left[\frac{1}{i!} \cdot \frac{\mathrm{d}^i}{\mathrm{d}n^i} \cos(n) \right] \Bigg|_{n=U_{\text{B,norm}}} \tag{3.4}$$

can be inspected. Here c_0 affects the strength of the optical carrier in the output signal $E_{\text{out}}(t)$. If the minimum transmission point U_{min} is chosen as bias voltage, an ideal Mach-Zehnder-modulator will completely suppress the optical carrier as $c_0 = 0$.

3.2.1.2 Erbium-Doped-Fiber Amplifier

Erbium-doped-fiber amplifiers are the most important class of optical fiber amplifiers as they amplify in the 1.55 μm wavelength range. A detailed introduction into optical amplifiers based on different gain media is given in [120].

In general, the gain of an optical amplifier is dependent on the signal's wavelength and the total input power fed to the amplifier. The frequency dependent gain coefficient $g_{\text{EDFA}}(\omega)$ is therefore given by

$$g_{\text{EDFA}}(\omega) = \frac{g_0}{1 + (\omega - \omega_0)^2 T^2 + P_{\text{tot}}/P_{\text{sat}}} \tag{3.5}$$

where g_0 is the peak gain value, ω_0 is the atomic transition frequency, T is the dipole relaxation time, ω is the optical frequency of the incident signal, P_{mean} is the mean input power of the amplifier and P_{sat} is its saturation power.

As the used signal bandwidth is small compared to the optical frequency, it can be assumed that the gain coefficient g is constant over the whole signal bandwidth. With this assumption eq. 3.5 can be rewritten as

$$g_{\text{EDFA}} = \frac{g_0}{k_\omega + P_{\text{mean}}/P_{\text{sat}}} \tag{3.6}$$

with

$$k_\omega = 1 + (\omega_{\text{center}} - \omega_0)^2 T^2 \tag{3.7}$$

where ω_{center} is the optical center frequency of the signals. It can be seen that the gain is dependent on the mean incident power P_{mean} of the amplifier not the instantaneous incident power.

In comparison to electrical amplifiers, which become nonlinear when driven close to the saturation, optical fiber amplifiers stay linear but the gain factor decreases if the mean of the incident power increases [120].

3.2.1.3 THz photodiodes and dual-polarization photomixer integration

Opto-electronic conversion in the 300 GHz band is one of the main limiting issues regarding high antenna feeding powers distributed via optical networks. Thus, optimization of the photodiode chips becomes a major aspect in the development of terahertz communication systems.

In this regard, a central role is taken by Indium Phosphide based photodiode layer structures. As a photodiode belonging to this category, an uni-travelling-carrier PD for optoelectronic conversion were used in this work since it offers comparatively high output powers in the frequency range of interest.

In contrast to other PD structures (such as pin-PDs or avalanche-PDs), UTC PDs include an additional p-doped absorption layer which forces a fast relaxation of the holes into the absorption layer itself. With regard to the achievable operating speed, the advantage of the absorption layer becomes clear. Since the electrons are the only carriers in the intrinsic layer a significant improvement of the PD's performance is achieved due to that the electrons have a much higher velocity than the holes [121].

By adding an additional not-intentionally-doped absorber, the UTC-PD can be extended to the so-called modified-uni-travelling-carrier (MUTC) or triple-transit-region (TTR) design [122]. Depending on the ratio between the depleted and undepleted absorber, the speed of the PDs can be enhanced through increasing the amount of drift current the carriers inherit. Beside this, the electric field in the depletion zone can be exactly adjusted by inserting doped cliff layers. This leads to another enhancement of carrier velocities.

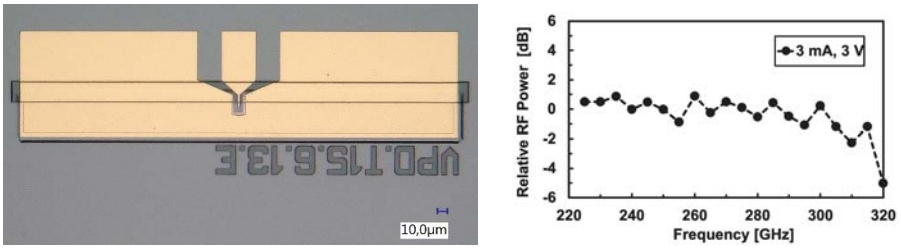

(a) (b)

Figure 3.4
(a) Photograph of the fabricated triple-transit-region photodiode, and its flat frequency response within J-band (b). From [122] © 2019 IEEE

At UDE, vertically illuminated TTR-PDs were developed which achieved a flat frequency response within the J-band of ± 1 dB from 220 GHz up to 300 GHz [122]. The flat frequency response is presented in Fig. 3.4.a together with a photograph of a fabricated TTR-PD (see Fig. 3.4.b). Furthermore, the introduced TTR-PDs reached an unsaturated RF-power of -18 dBm at 300 GHz biased with a voltage of -4 V.

In order to better exploit the developed PD chips in complex experimental setups, UDE has investigated novel integration concepts. This has already led to small series prototype for mm-wave coherent photonic mixing for RoF applications, which is shown in Fig. 3.5.a. As outlined in [123], the utilization of a coherent photonic mixer (CPX) has several advantages compared to just use a single photodiode.

In principle, a CPX consists of a pair of PDs – also called balanced photodiode (BPD) – each supplied by one output of a 2x2 multimode interference (MMI) coupler. Using this approach offers the opportunity to perform heterodyning of two optical input signals whereas one of them act as a local oscillator. At the same time the theoretical RF output power is increased by 6 dB, thanks to the avoidance of classical 3 dB losses in case of feeding a single PD. Moreover, the differential wiring of the BPD results in a significantly lower noise level since the DC-terms of each PD are canceled out. Apart from this, the utilization of an integrated CPX with rectangular waveguide output is capable to serve as an integration platform for Fiber-to-the-Antenna applications and therefore enables direct optical-to-wireless conversion.

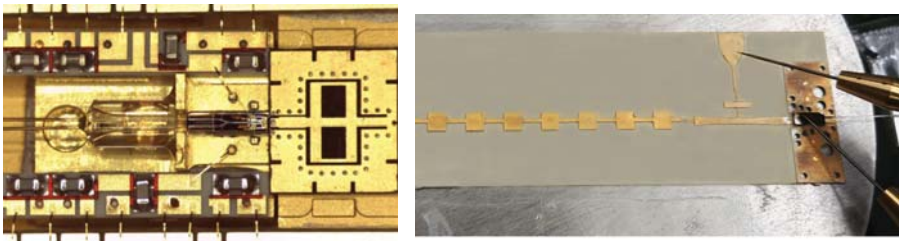

(a) (b)

Figure 3.5
Photograph of the fabricated CPX with integrated power amplifier and WR12 output (a) and beam steering polarization diversity photoreceiver fed by fiber-chip coupling (b)

In combination with frequency steering antennas – such as leaky-wave antennas – even optically controlled beam steering can be realized, since the RF can be adjusted by tuning the LO-laser. Thus, a multi-user wireless communication system based on dense wavelength division multiplexing can be implemented as multiple beams with different spatial directions are generated performing frequency-space mapping [124, 125].

Opto-electronic packaging provides vast potential for offering added functionality by integrating photonic with RF components. We have demonstrated this with an integrated beam steering polarization diversity photoreceiver (PDP), which is depicted in Fig. 3.5.b. Besides increasing the occupied spectrum or using higher-order modulation methods dual-polarization transmission is able to effectively double the capacity of a communication link [126].

Since both polarizations are distributed via the same CRoF link the necessity of a polarization diversity photoreceiver for opto-electronic conversion is obvious. In principle, such a PDP consists of two waveguide photodiodes which are fed by either the transversal electric (TE) or the transversal magnetic (TM) part of the transmitted signal. Therefore, a separation of both polarizations is needed and carried out through a monolithic integrated polarization beam splitter (PBS) which exploits the so called 'mode sorting effect'.

Placing a multimode waveguide next to a monomode waveguide leads to an evanescent coupling of the TE-polarized light into the multimode section causing the desired polarization splitting [127]. Furthermore, the utilization of a PDP is best suited for Fiber-to-the-Antenna applications since it provides an embedded spot-size converter which simplifies fiber-chip coupling significantly [125].

3.2.1.4 Schottky-Barrier Diode Envelope Detector

Phase-noise insensitive Schottky-barrier diodes are utilized for THz down-conversion. They operate over a large bandwidth only limited by their rectangular waveguide interface and do not require frequency drift compensation between the transmitter and receiver LOs. As they perform envelope detection, the data signal needs to provide an IF carrier – enabling down-conversion to IF instead of baseband – to retain the phase information.

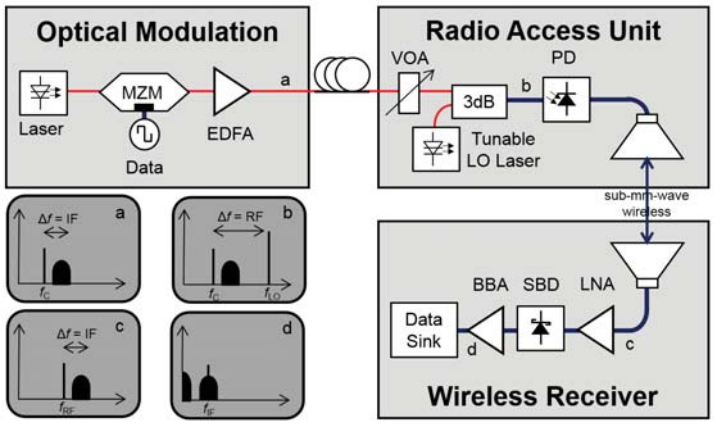

Figure 3.6
Analog architecture of the employed coherent Radio-over-Fiber THz Transmission system with indicated signal spectra

This is necessary for higher order modulation and is a focus of this project for optimizing the spectral efficiency of the system: Due to the square law detection, down-conversion is employed to baseband as well as IF, creating

the potential for signal-to-signal beat interference (SSBI). Also the transmitter has to relocate power from the signal to transmit the carrier.

While envelope detection requires power in the IF carrier and has a higher conversion loss than heterodyne detection with a high power LO, it is less complex and inexpensive due to the used SBDs. The analog architecture of the utilized transmission system using a SBD receiver is depicted in Fig. 3.6. The signal spectra illustrate the ideal modulation and up-/down-conversion processes. It can be seen, that for small IFs and high BWs SSBI occurs in the down-converted IF-OFDM signal. This can be fundamentally avoided by using an IF equal to 1.5 times the BW. But then the transmission and baseband receiver bandwidth needs to be doubled, resulting in a significantly reduced spectral and cost efficiency.

3.2.2 Transmission System Modeling

In order to optimize the transmission performance of the outlined system, components and the comprised sub-systems are simulated based on modeling from analytical as well as measured behavior. Thereby, the focus lies in operating point optimization and system linearization. Especially the transmitter side is relevant to this approach because here compensation can be applied without needing to know the channel parameters.

3.2.2.1 Transmitter Model

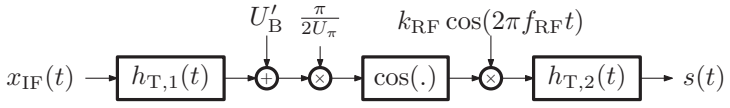

Figure 3.7
Block diagram of the transmitter model

The mathematical model of the transmitter is illustrated in form of the schematic in Fig. 3.7. The real-valued input signal $x_{\mathrm{IF}}(t)$ is convolved with an impulse response $h_{\mathrm{T},1}(t)$. The impulse response $h_{\mathrm{T},1}(t)$ combines the frequency selective behaviors of the power amplifier and the Mach-Zehnder-modulator's input stage. An offset $U'_{\mathrm{B}} = U_{\mathrm{B}} - U_{\max}$ is added to the signal. Here, U_{B} is the bias voltage of the Mach-Zehnder-modulator and $U_{\max}$ is the voltage which corresponds to the maximum-transmission point. The signal is then scaled to fit the nonlinear characteristics as given in section 3.2.1.1.

Afterwards the signal is transmitted over the MZM's cosine-shaped nonlinear characteristic. It is assumed that the bandwidth of the signal is small compared to the available optical bandwidth. Therefore the optical components do not show frequency selectivity inside the used band. Under these conditions the optical part of the system can be simplified.

In the model, the non-linear distorted signal is then up-converted to the

radio frequency f_{RF}. The frequency f_{RF} of the radio carrier is given by the difference between the frequencies of both optical carriers provided by the two lasers. The amplitude of the radio carrier A_{RF} results from the optical components due to the performed photonic up-conversion. The up-converted signal is then convolved with the impulse response $h_{\mathrm{T},2}(t)$ to form the transmit signal $s(t)$. The impulse response $h_{\mathrm{T},2}(t)$ models the frequency selective behavior of the photodiode's output stage as well as frequency selective behavior of the transmitting antenna. The transmit signal $s(t)$ can be derived as

$$s(t) = A_{\mathrm{RF}} h_{\mathrm{T},2}(t) * \left[\cos(2\pi f_{\mathrm{IF}} t) \cos\left(\frac{\pi}{2U_\pi} \left(U'_{\mathrm{B}} + h_{\mathrm{T},1}(t) * x_{\mathrm{IF}}(t) \right) \right) \right] \tag{3.8}$$

with

$$A_{\mathrm{RF}} = \frac{\hat{E}_1 \hat{E}_2 \sqrt{k_{\mathrm{T}} g_{\mathrm{EDFA}}}}{2}. \tag{3.9}$$

The factor A_{RF} is composed of the amplitudes $\hat{E}_1$ and $\hat{E}_2$ of the carrier signal of both lasers, the transmission coefficient k_{T} of the Mach-Zehnder-modulator and the gain coefficient g_{EDFA} of the erbium-doped-fiber amplifier.

By using the Taylor-series expansion, eq. 3.8 can be rewritten as

$$s(t) = A_{\mathrm{RF}} h_{\mathrm{T},2}(t) * \left[\cos(2\pi f_{\mathrm{IF}} t) \sum_{i=0}^{\infty} c_i \left(h_{\mathrm{T},1}(t) * x_{\mathrm{IF}}(t) \right)^i \right] \tag{3.10}$$

with

$$c_i = \left[\frac{1}{i!} \cdot \frac{\mathrm{d}^i}{\mathrm{d}n^i} \cos(n) \right] \Bigg|_{n=\frac{\pi(U_{\mathrm{B}} - U_{\max})}{2U_\pi}}. \tag{3.11}$$

Now the transmit signal $s(t)$ can be split into three components

$$s_{\mathrm{c}}(t) = c_0 A_{\mathrm{RF}} \left| H_{\mathrm{T},2}(2\pi f_{\mathrm{RF}}) \right| \cos(2\pi f_{\mathrm{IF}} t), \tag{3.12}$$

$$s_{\mathrm{s}}(t) = c_1 A_{\mathrm{RF}} h_{\mathrm{T},2}(t) * \left[\cos(2\pi f_{\mathrm{RF}} t) \left(h_{\mathrm{T},1}(t) * x_{\mathrm{IF}}(t) \right) \right], \tag{3.13}$$

$$s_{\mathrm{I}}(t) = A_{\mathrm{RF}} h_{\mathrm{T},2}(t) * \left[\cos(2\pi f_{\mathrm{RF}} t) \sum_{i=2}^{\infty} c_i \left(h_{\mathrm{T},1}(t) * x_{\mathrm{IF}}(t) \right)^i \right]. \tag{3.14}$$

in such a way that $s_{\mathrm{c}}(t)$ gives the radio frequency carrier signal, $s_{\mathrm{s}}(t)$ gives the linear component of the signal and $s_{\mathrm{I}}(t)$ gives signal-to-signal beat-interference terms.

$$s(t) = s_{\mathrm{c}}(t) + s_{\mathrm{s}}(t) + s_{\mathrm{I}}(t) \tag{3.15}$$

Fig. 3.8 shows both the power spectral density of the signal $x_{\mathrm{IF}}(t)$ at the input of the transmitter in subplot a) as well as of the signal $s(t)$ at the output of the transmitter in subplot b). A 10 GHz wide OFDM signal at an intermediate frequency of 15 GHz is chosen as an input to the transmitter.

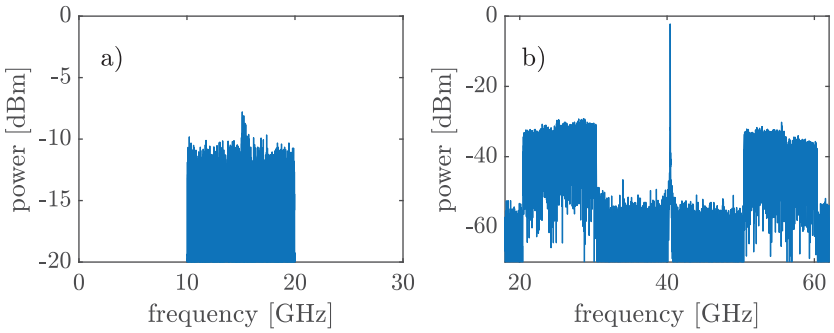

Figure 3.8
Ideal power-spectral-density of a 10 GHz wide OFDM signal at an intermediate-frequency of $f_{\mathrm{IF}} = 15\,\mathrm{GHz}$ as the input signal to the Mach-Zehnder-modulator (a) and measured power-spectral-density of the output signal of the transmitter with $f_{\mathrm{RF}} = 40\,\mathrm{GHz}$ (b)

The intended radio frequency f_{RF} of 40 GHz is chosen as this allows capturing the signal with a 160 GSa/s digital sampling oscilloscope. The Mach-Zehnder-modulator was biased close to the minimum-transmission point.

At the minimum-transmission point, the carrier is mostly suppressed and the Mach-Zehnder-modulator behaves approximately linear. For this reason the carrier component $s_{\mathrm{c}}(t)$ of the output signal as well as the signal component $s_{\mathrm{s}}(t)$ are clearly visible while the interference component $s_{\mathrm{I}}(t)$ cannot be observed.

3.2.2.2 Receiver Model

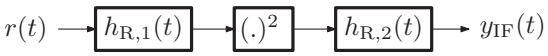

Figure 3.9
Block-diagram of the receiver model

The mathematical model of the coherent detection receiver is shown in the schematic in Fig. 3.9. The received signal $r(t)$ at the input of the receiving antenna is convolved with the impulse response $h_{\mathrm{R},1}(t)$. The impulse response $h_{\mathrm{R},1}(t)$ models the frequency-selective behaviors of the receiving antenna, the first low-noise amplifier and the input stage of the used Schottky-barrier diode detector.

The signal is then squared to model the square-law characteristics of the Schottky-barrier diode detector before the signal is transferred via the impulse response $h_{\mathrm{R},2}(t)$ to the output. The impulse response $h_{\mathrm{R},2}(t)$ models the

frequency selective behavior of the Schottky-barrier diode detector and the second low-noise amplifier.

The signal $y_{\mathrm{IF}}(t)$ at the output of the receiver depends upon the received signal $r(t)$ according to:

$$y_{\mathrm{IF}}(t) = h_{\mathrm{R},2} * \left(r(t) * h_{\mathrm{R},1}\right)^2 . \tag{3.16}$$

3.2.2.3 System Model

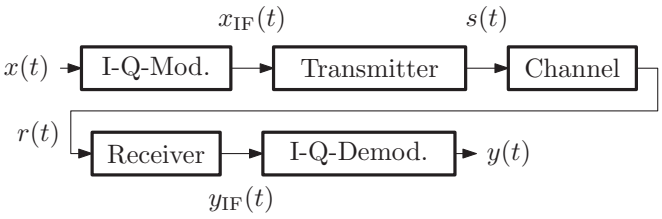

Figure 3.10
Model of the complete transmission system

The model of the complete transmission system is shown in Fig. 3.10. The transmitter hardware described in section 3.2.2.1 is preceded by an I-Q-modulator. This allows the system's input signal $x(t)$ to be complex-valued. The I-Q-modulator up-converts the input signal to an intermediate frequency f_{IF}. The signal $x_{\mathrm{IF}}(t)$ at the output of the I-Q-modulator is then real-valued and used as input signal to the transmitter. The transmitter up-converts the signal $x_{\mathrm{IF}}(t)$ to the desired radio frequency f_{RF} forming the output signal $s(t)$.

The output signal $s(t)$ of the transmitter is then transmitted over the channel, which is assumed to be frequency-selective and is modeled by the channel impulse response $h_{\mathrm{c}}(t)$. The output signal $r(t)$ of the channel is then used as input to the receiver as described in section 3.9 to form the down-converted output signal $y_{\mathrm{IF}}(t)$. By I-Q-demodulation the real-valued signal $y_{\mathrm{IF}}(t)$ at the intermediate-frequency is converted to a complex-valued baseband signal $y(t)$. It holds for the input signal $x_{\mathrm{IF}}(t)$ to the transmitter and for the output signal $y(t)$ of the system:

$$x_{\mathrm{IF}}(t) = \frac{1}{2} x(t) \mathrm{e}^{\mathrm{j}2\pi f_{\mathrm{IF}} t} + \frac{1}{2} x^*(t) \mathrm{e}^{-\mathrm{j}2\pi f_{\mathrm{IF}} t} \quad \text{and} \tag{3.17}$$

$$y(t) = h_{\mathrm{LP}}(t) * \left(y_{\mathrm{IF}}(t) \mathrm{e}^{-\mathrm{j}2\pi f_{\mathrm{IF}} t}\right) . \tag{3.18}$$

First, the relation between the output signal $y_{\mathrm{IF}}(t)$ of the transmission system's hardware and the input signal $x_{\mathrm{IF}}(t)$ is shown. Here $h_{\mathrm{LP}}(t)$ is a low-pass filter that lets only the signal bandwidth pass. This relation is then extended by the I-Q-modulation steps to give a relation between the input signal $x(t)$ and output signal $y(t)$ of the complete system.

It can be shown that the output signal $y_{\mathrm{IF}}(t)$ depends on the input signal $x_{\mathrm{IF}}(t)$ in the following way:

$$\begin{aligned} y_{\mathrm{IF}}(t) =& A_{\mathrm{RF}}^2 \cdot h_{\mathrm{R},2}(t) * \\ & * \left[\left(\cos\left(\frac{\pi}{2U_\pi} (h_{\mathrm{T},1}(t) * x_{\mathrm{IF}}(t) + U'_{\mathrm{B}}) \right) \cos(2\pi f_{\mathrm{RF}} t) \right) * h_2(t) \right]^2 \end{aligned} \tag{3.19}$$

with

$$h_2(t) = h_{\mathrm{T},2}(t) * h_{\mathrm{c}}(t) * h_{\mathrm{R},1}(t). \tag{3.20}$$

The impulse response $h_2(t)$ is introduced to combine the series of impulse responses $h_{\mathrm{T},2}(t)$ at the output of the transmitter, $h_{\mathrm{c}}(t)$ of the channel and $h_{\mathrm{R},1}(t)$ at the input of the receiver.

As described in eq. 3.6 the gain coefficient g_{EDFA} of the Erbium-doped-fiber amplifier is dependent on the total incident power P_{tot}, which can be calculated from the optical output signal $E_{\mathrm{out}}(t)$ from eq. 3.3 as

$$P_{\mathrm{tot}} \propto \left\langle \left| E_{\mathrm{out}}^2(t) \right| \right\rangle. \tag{3.21}$$

Making use of the Taylor-series expansion, eq. 3.19 can be rewritten around the bias point as

$$\begin{aligned} y_{\mathrm{IF}}(t) =& A_{\mathrm{RF}}^2 \cdot h_{\mathrm{R},2}(t) * \\ & * \left[\left(\sum_{i=0}^{\infty} c_i (h_{\mathrm{T},1}(t) * x_{\mathrm{IF}}(t))^i \cos(\omega_{\mathrm{RF}} t) \right) * h_2(t) \right]^2 \end{aligned} \tag{3.22}$$

with

$$c_i = \left[\frac{1}{i!} \cdot \frac{\mathrm{d}^i}{\mathrm{d}n^i} \cos(n) \right] \Bigg|_{n = \frac{\pi(U_{\mathrm{B}} - U_{\max})}{2U_\pi}}. \tag{3.23}$$

By analyzing eq. 3.22, the linear component of the signal can be extracted as

$$y_{\mathrm{IF},1}(t) = \frac{\pi A_{\mathrm{RF}}^2 c_0 c_1 |H_2(\omega_{\mathrm{RF}})|}{2U_\pi} x_{\mathrm{IF}}(t) * h_{\mathrm{g}}(t) \tag{3.24}$$

with

$$h_{\mathrm{g}}(t) = h_{\mathrm{T},1}(t) * (h_2(t) \mathrm{e}^{\mathrm{j}\omega_{\mathrm{RF}} t} + h_2(t) \mathrm{e}^{-\mathrm{j}\omega_{\mathrm{RF}} t}) * h_{\mathrm{R},2}(t). \tag{3.25}$$

From this result, the linear relation between the complete system's input signal $x(t)$ and the linear component $y_1(t)$ of the complete system's output signal $y(t)$ can be calculated using eq. 3.17 and eq. 3.18

$$\begin{aligned} y_1(t) =& \left[\left(\left(\frac{1}{2} x(t) \mathrm{e}^{\mathrm{j}2\pi f_{\mathrm{IF}} t} + \frac{1}{2} x^*(t) \mathrm{e}^{-\mathrm{j}2\pi f_{\mathrm{IF}} t} \right) * h_{\mathrm{g}}(t) \right) \cdot 2\mathrm{e}^{-\mathrm{j}2\pi f_{\mathrm{IF}} t} \right] * \\ & * h_{\mathrm{LP}}(t) \cdot k_{\mathrm{lin}} \end{aligned} \tag{3.26}$$

with

$$k_{\text{lin}} = \frac{\pi A_{\text{RF}}^2 c_0 c_1 |H_2(\omega_{\text{RF}})|}{2U_\pi}. \tag{3.27}$$

With the assumption that $h_{\text{LP}}(t)$ is the impulse response of a perfect low-pass filter that suppresses any component above the signal bandwidth, eq. 3.26 can be simplified to

$$y_1(t) = k_{\text{lin}} x(t) * \left(h_{\text{g}}(t) \mathrm{e}^{-\mathrm{j}2\pi f_{\text{IF}} t}\right). \tag{3.28}$$

3.2.3 Simulation and Optimal Parameter

The system described in section 3.2.2.3 is implemented in MATLAB® with parameters taken from the physical setup.

In a simulation, the parameters f_{IF}, U_{B} and the power $P_{\text{x}_{\text{IF}}}$ of the input signal $x_{\text{IF}}(t)$ are analyzed through simulation to find the set for which the error-vector magnitude (EVM) is minimal. For this a 10 GHz OFDM signal with 64 carrier is simulated. A Zadoff-Chu sequence is used as a preamble for training before 10 OFDM data symbols are transmitted. Equalization is done by using zero-forcing.

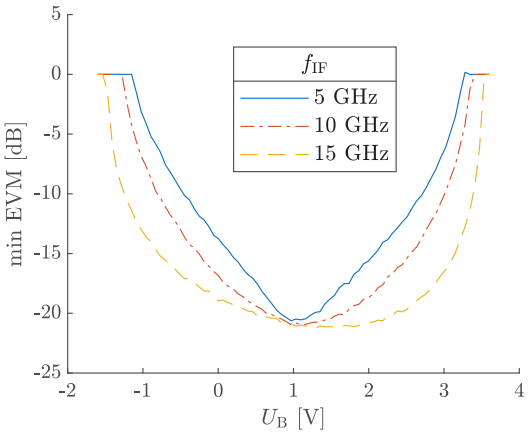

Figure 3.11
Lowest EVM over the bias voltage, maximum-transmission point is at -1.6 V and minimum-transmission point is at 3.6 V. From [128] © 2020 IEEE

The error-vector magnitude m_{EVM} serves as figure of merit for the simulated signal. The error-vector $\vec{e}$ is calculated from the vector of normalized sent constellation points $\vec{s}$ and the normalized received constellation points $\vec{r}$ after equalization, but before detection, as

$$m_{\text{EVM}}(\text{dB}) = 10 \cdot \log_{10}\left(|\vec{s} - \vec{r}|^2\right). \tag{3.29}$$

The simulated minimal attainable EVM values considering all input powers P_{xIF} are plotted over varying bias voltages U_{B} in Fig. 3.11. In contrast, Fig. 3.12 shows the minimal simulated EVM of all bias voltages U_{B} over the input power P_{xIF} for f_{IF}=5 GHz and a signal bandwidth BW=10 GHz.

In Fig. 3.11 it can be observed that bias voltages U_{B} close to the maximum-transmission point at -1.6 V exhibit high EVM values. This is due to the fact that most power is allocated to the carrier and the sidebands are weak. This leads to the linear component $y_1(t)$ of the output signal being small compared to the noise level of the system. The EVM decreases when moving the bias voltage towards the minimum-transmission point as more power gets allocated to the sideband lifting the output signal's power over the noise level.

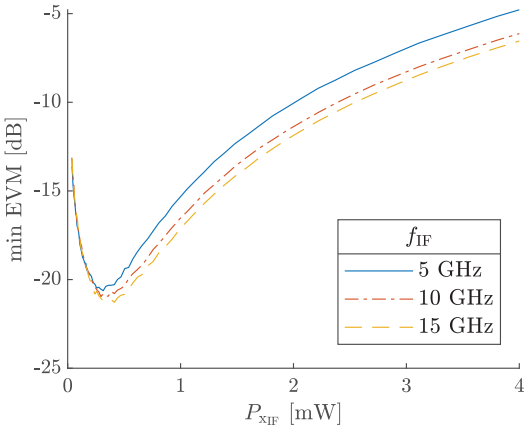

Figure 3.12
Lowest EVM over the signal power P_{x}

The EVM reaches a minimum of -20.6 dB at a bias voltage U_{B} of 1 V for an intermediate frequency f_{IF} 5 GHz, -21 dB at 1.16 V for 10 GHz and -21.3 dB at 1.3 V for 15 GHz. It can be observed, that with increasing intermediate frequency f_{IF} the EVM for bias voltages closer to the minimum-transmission point U_{min} at 3.6 V produce lower values of EVM. With higher intermediate frequencies f_{IF} an increasing portion of the nonlinear distortion does not overlap with the signal bandwidth. This affects especially the quadratic distortion caused by the receiver and as a result the EVM for bias voltages closer to the minimum transmission point at 3.6 V decreases.

In Fig. 3.12 the dependency of the EVM at the output of the system on the power P_{x} is shown. The trade-off between noise-limited and interference-limited EVM can clearly be observed. For input powers P_{xIF} smaller 0.5 mW the system is limited by the noise at the output of the receiver.

The minimum simulated EVM is -20.6 dB at an input power P_{xIF} 0.3 mW for an intermediate frequency f_{IF} = 5 GHz, -21 dB at P_{xIF} = 0.33 mW for f_{IF}

10 GHz and -21.3 dB at P_{xIF} =0.4 mW for f_{IF} = 15 GHz. For higher input powers P_{xIF} the EVM is mainly limited by interference. As mentioned before, interference is lower for higher intermediate frequencies f_{IF}. This can also be observed in the graphs for input powers P_{xIF} higher than 0.4 mW.

3.3 Wireless mm-wave and THz Channels

As outlined in the introduction, larger bandwidth channels are key for realizing the data rates demanded for new use cases and applications of 5G and beyond. Especially, the goal of 100 Gbit/s wireless transmission would require an extension of spectral efficiency of nowadays systems to 14 bit/s/Hz [129]. The difficulty of this approach fuels the desire for more bandwidth available in the (sub-)mm-wave and THz bands. At these frequency bands even Tbit/s data rate links are imaginable without striving for unfeasible modulation formats by taking advantage of the huge yet unexploited bandwidth.

However, the distinct propagation challenges at such high frequencies need to be considered. At THz frequencies, signals suffer significant power attenuation due to atmospheric attenuation [130] as well as an increased free-space path loss (FSPL). In addition, surface roughness could play an important role in both specular reflection and diffuse scattering [131].

In practice, no surface is completely smooth, and the surface roughness causes progressive attenuation of the power in the specular scattering. Such effect would impact the overall system performance, especially in the case of non-line-of-sight (NLoS) scenarios where the received power depends entirely on the reflected paths.

Therefore, channel estimation plays a significant role to enable reliable and high performance communication at these frequencies. The substantial channel bandwidths in excess of 10 GHz are expected to not be flat and cause great challenges for channel estimation and subsequent signal processing. Thus, channel sounding and measurement experiments are vital for understanding THz communication better and succeeding in 100 Gbit/s transmission demonstrations.

3.3.1 Channel Sounding Experiments

Many approaches can be implemented for generating THz waves, yet the most successful ones are the up-conversion from mm-wave frequencies using frequency multiplication, and the down-conversion from optical frequencies [132]. For the channel sounding experiments, the first approach is employed, as it is supported by commercial measurement equipment with high dynamic range.

Several studies focused on the THz channel characterization can be found in the literature. The first of its kind channel measurements at 300 GHz with

10 GHz of bandwidth are given in [133] with line-of-sight (LoS) and non-line-of-sight (NLoS) scenarios in an indoor environment, where in [134] the LoS THz measurements are reported over a 240–300 GHz frequency range in an anechoic chamber with distances up to 80 cm. Path loss models at 300 GHz LoS desktop channel with distances up to 70 cm and over 20 GHz of bandwidth are reported in [135].

3.3.1.1 Measurement Equipment

The main equipment in our measurement setup is the R&S ZVA67 vector network analyzer (VNA), which has an upper frequency limit of 67 GHz, in addition to two R&S ZC330 mm-wave converters that are employed at both Tx and Rx sides, with a typical dynamic range of 115 dB.

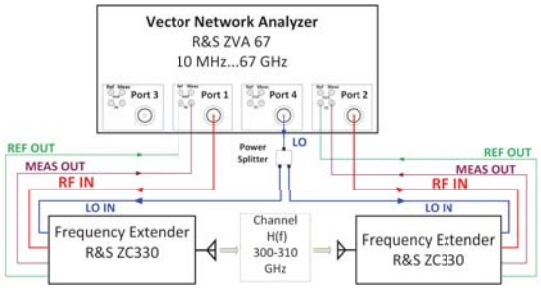

Figure 3.13
Block diagram of the measurement equipment setup. From [136] © 2019 IEEE

The ZC330 contains a frequency multiplier (× 18) to transform the RF signal from the VNA port (16.67 GHz to 17.22 GHz) to our targeted frequency range (240 GHz to 300 GHz), and two harmonic mixers for down-conversion of the measurement (MEAS) and reference (REF) signals.

Table 3.1
Measurement parameters. From [136] © 2019 IEEE

Parameter	Value
Frequency points	801
IF filter bandwidth	10 kHz
Center frequency	270 GHz
Start frequency	240 GHz
Stop frequency	300 GHz
Bandwidth	60 GHz
Maximum excess delay	13.34 ns
Frequency step size	75 MHz

The local oscillator signal is derived from the internal oscillator of the VNA

through one test port of the VNA followed by a power splitter to provide the LO signal for both converters. Horn antennas are installed at the test port adapters of each converter through their waveguide flanges.

A two-port TOSM (through, open, short, match) calibration is executed on the converter's waveguide ports considering our experiment parameters. The measurement is conducted over 60 GHz of bandwidth, with 801 frequency points. Further experiment parameters are given in Table 3.1, and a block diagram of the experimental setup is shown in Fig. 3.13.

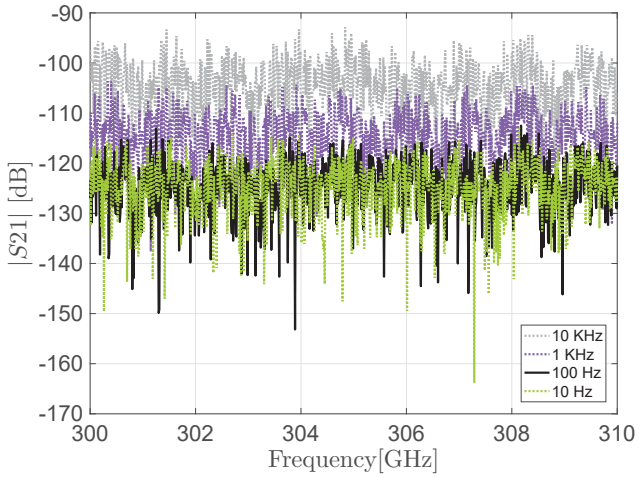

Figure 3.14
Equipment noise power at different IF filter bandwidth values. From [136] © 2019 IEEE

The noise power of the measurement equipment is measured by connecting a short connector to the converter's waveguide antenna of Tx side and a match connector to the converter's waveguide antenna of Rx side. The equipment noise power decreases when lower bandwidths are used for the IF filter as illustrated in Fig. 3.14. It is worth mentioning, that the channel measurement time of one sweep increases by decreasing the IF filter bandwidth, resulting in a trade-off between measurement accuracy and time.

3.3.1.2 Measurement Environment

The measurement setup is installed in a $7.9 \times 6.5\ \mathrm{m}^2$ lecture room in the Institute of Digital Signal Processing (DSV) at the University of Duisburg-Essen, where the LoS is realized on top of a sequence of $140 \times 70\ \mathrm{cm}^2$ wooden tables with 70 cm height above the ground. To ensure the alignment of the converters, they were placed in a way that the center point of both converters' waveguide is located at a distance of 21 cm from the side edge of the table.

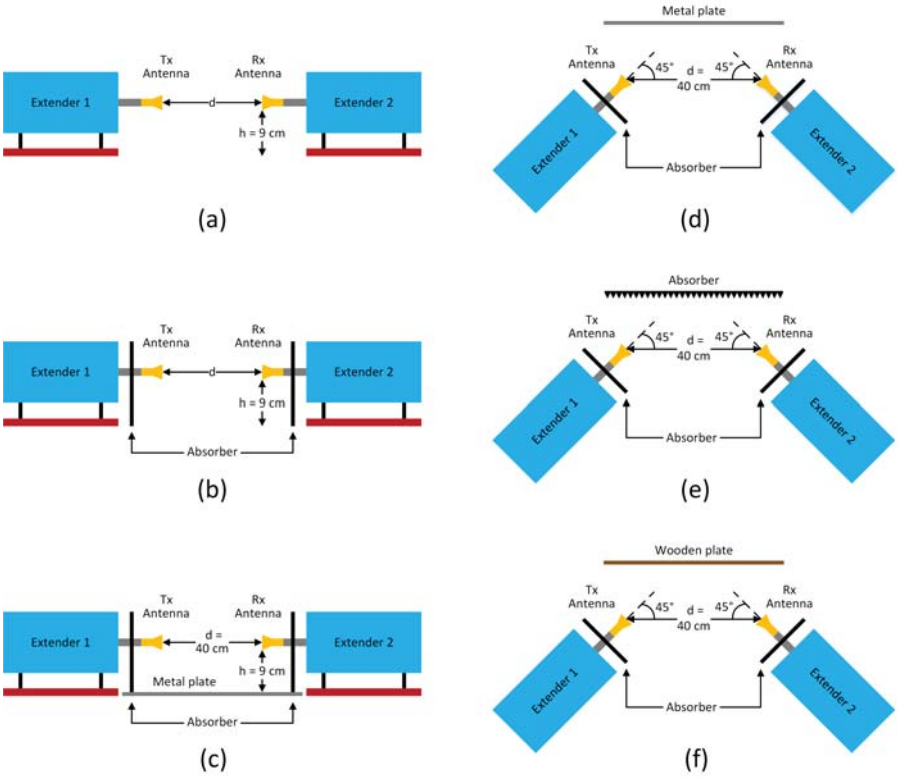

Figure 3.15
The conducted measurements scenarios for both LoS (left) and NLoS cases (right)

3.3.1.3 Measurement Scenarios

The different channel measurement scenarios investigated during the measurement campaign are illustrated in Fig. 3.15.

Scenario A (LoS): No absorbers are implemented and the measurements were taken for different Tx-Rx separation distances.

Scenario B (LoS with absorbers): Two absorbers at both Tx and Rx converters were placed to minimize the reflections from the metallic enclosure of the converters. Measurements are also taken for different Tx-Rx separation distances.

Scenario C (LoS with metal plate): A metal plate is placed underneath the LoS between the Tx and Rx converters.

Scenario D, E and F represent the NLoS cases using a metal plate, an absorber or a wooden plate as reflectors.

3.3.2 Channel Properties and Modeling

3.3.2.1 Channel Characteristics

Channel transfer function
The channel transfer function (CTF) is represented by the measured transmission coefficient S_{21} recorded in the frequency domain, which is calculated using the complex IQ data extracted from the VNA using the following formula, where A is the amplitude, and θ is the phase in radians:

$$S_{21}[\mathrm{dB}] = 20 \cdot \log_{10}(\mathrm{abs}(IQ)) \tag{3.30}$$

$$IQ = A\cos(\theta) + \mathrm{j}A\sin(\theta) \tag{3.31}$$

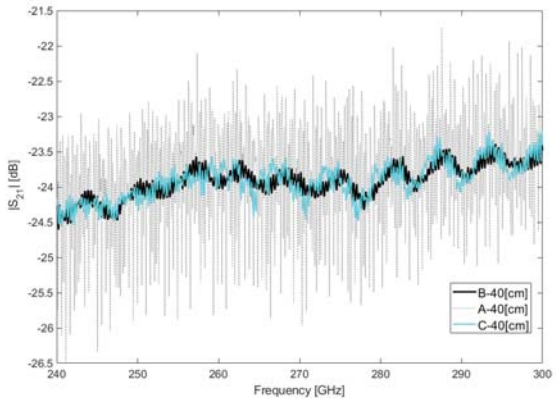

Figure 3.16
The measured reflection coefficient S_{21} in case of LOS scenarios A, B and C

The resulting CTFs for scenarios A, B and C are displayed in Fig. 3.16. They are derived by averaging across 50 measurement snapshots corresponding to 50 measurement sweeps of the VNA.

Power delay profile
The power delay profile (PDP) provides the distribution of the signal power received over a multipath channel as a function of the propagation delay. Thereby the signal power of each multipath is plotted against its respective propagation delay. The PDP is obtained as the spatial average of the complex channel impulse response. It can be calculated using the scattering parame-

ters by taking the inverse fast Fourier-transformation (IFFT) of the channel response in the frequency domain.

The time domain delay range TD_{range} is the inverse of the frequency step-size of the measurement in frequency domain and is calculated by:

$$TD_{\text{range}} = \frac{N_{\text{P}} - 1}{BW} \tag{3.32}$$

N_{P} is the number of frequency points (801), and BW is the total measurement channel bandwidth (60 GHz), resulting a time domain range between 0 and 13.33 ns for our measurement scenarios.

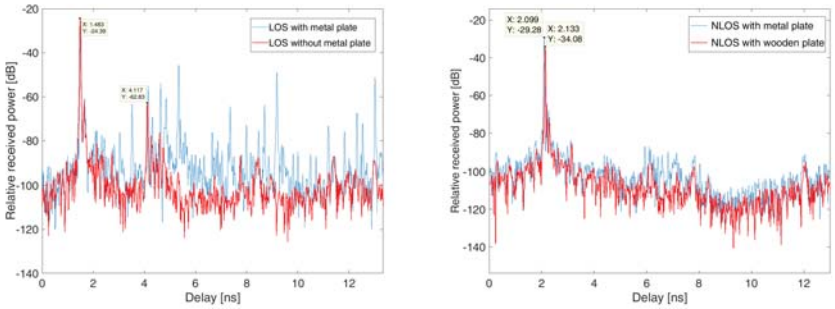

(a) (b)

Figure 3.17
Power delay profile under LoS conditions for scenarios B and C (a) and under NLoS conditions for scenarios D and F (b)

In Fig. 3.17.a the PDP obtained from scenario B and C are compared; it can be clearly seen how the presence of the absorbers behind the antennas has blocked many of the MPCs, which are a result of reflections from the metallic body of the frequency converters. Nevertheless, we can see some MPCs which the absorbers could not block, such as the MPC which is caused due to reflection from the body of the antenna itself.
Fig. 3.17.b shows a comparison of PDP in NLoS scenarios when the rays are specularly reflected. The highest peak corresponds to the first NLoS specular reflection from the metal plate in scenario D and from the wooden plate in scenario F. It can be observed that the wooden plate induces higher path loss compared to the metal plate (6 dB difference in the highest peak), because the metal has better reflection properties. It is also obvious how the metal plate causes new MPCs corresponding to second reflections from the table.

3.3.2.2 Channel Modeling

The realization of THz wireless communication systems requires reliable indoor channel modeling and measurements in order to employ available infor-

mation about the terahertz channel. The existing channel models for lower frequency bands cannot be used for THz channels because of its principally higher absolute bandwidth as well as a significant higher temporal resolution of the channel multipath components. Moreover, a larger free space path loss due to smaller antenna apertures, a frequency dependent atmospheric attenuation, severe material attenuation and dispersive material reflections makes the propagation characteristics different at THz frequencies.

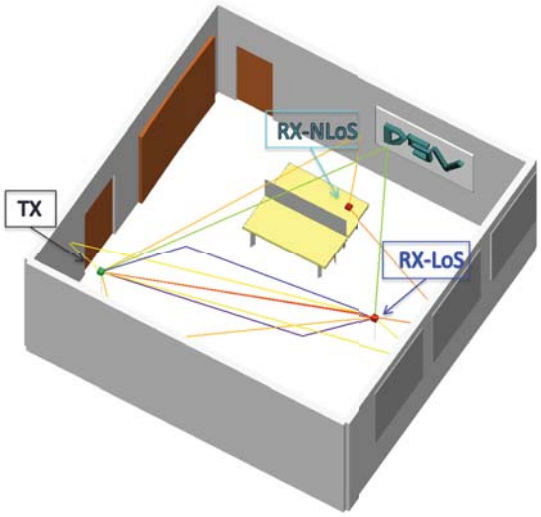

Figure 3.18
3D layout of the simulated office environment. From [130] © 2019 IEEE

Indoor channel models can be categorized into analytical or statistical models. Concerning deterministic channels, site specific ray-tracing models are mostly applied. For THz communication, the models are based on geometrical optics, in which both the LoS and NLoS wave propagation paths are investigated. However, the commercial available ray-tracer tools are incapable to consider the atmospheric attenuation above 100 GHz.
In order to overcome this problem, the frequency-dependent atmospheric attenuation models are implemented based on their analytical description from the International Telecommunication Union (ITU)[130].

The frequency dependent complex impulse response of the channel has been computed with the corresponding number of paths, angle-of-arrival (AoA), angle-of-departure (AoD) and time-of-arrival (ToA) to obtain meaningful results. Fig. 3.18 shows the indoor simulation setup, and Fig. 3.19 presents the channel transfer function considering the atmospheric attenuation in both LoS and NLoS cases.

Despite the growing literature on THz band, there is still a lack of proper channel models based on power delay profile at this spectrum band.

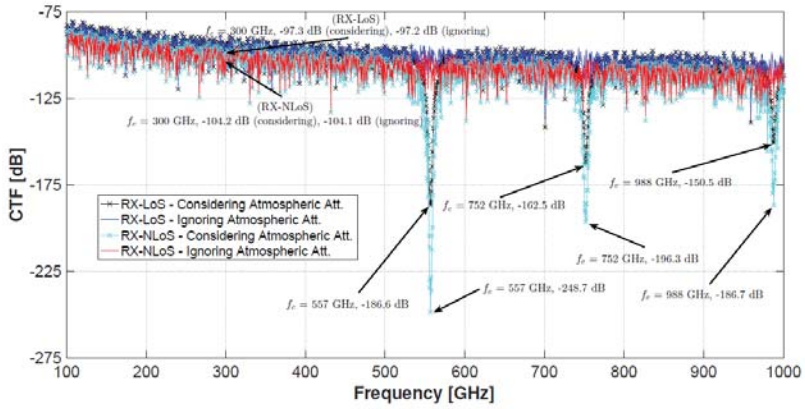

Figure 3.19
The channel transfer function with and without considering the atmospheric attenuation. From [130] © 2019 IEEE

Table 3.2
Communication channels comparison. From [136] © 2019 IEEE

Conventional vs. THz Channel				
Band	2.4 GHz	60 GHz	300 GHz	1 THz
Bandwidth	80 MHz	7–14 GHz	∼ 50 GHz	up to 110 GHz
Path loss at 5 m	∼ 54 dB	∼ 82 dB	∼ 96 dB	∼ 106 dB
Data rate	600 Mbps	∼ 8 Gbps	∼ 100 Gbps	> 100 Gbps

Therefore, we have also investigated the impact of different sounding bandwidths, center frequencies and transmit power on PDP at THz frequencies. Atmospheric attenuation and free space path loss, limit the signal transmission distance and coverage range to inroom scenarios. The FSPL at 300 GHz is much stronger than at lower frequencies as listed in Table 3.2 and thus requires highly directional antennas to combat the propagation losses. The data rates for 2.4 GHz and 60 GHz given in the table are based on the Wi-Fi IEEE 802.11-ax and -ay standards.

3.4 High Bandwidth OFDM Measurement System

The approach of the Tera50+ fiber-wireless transmission system aims at delivering a transparent transmitter and receiver. By means of RoF techniques and IF-OFDM signals, a simple transparent envelope detection receiver is re-

alized and complexity is shifted to the transmitter. This allows to model and optimize the transmission system more effectively, as the channel does not need to be known for its non-linear compensation.

So the introduced fiber-wireless transmission system can be employed to test and measure digital modulation schemes under real-life conditions. As both the transmitter and receiver begin/end in the digital domain, different modulation types and waveforms can be changed and measured flexibly. Thereby, a large bandwidth of up to 40 GHz per channel can be used and multi-channel transmission is also possible through optical multiplexing techniques.

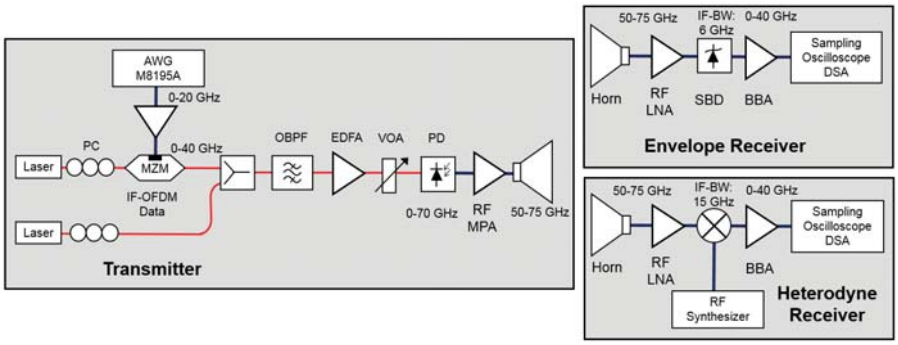

Figure 3.20
System setup used for the 60 GHz transmission measurements with envelope detector (top right) and heterodyne mixer receiver (bottom right)

The employed OFDM system further contains a Zadoff-Chu sequence preamble, which is utilized for channel estimation. Through the scalable photonic up-conversion and the transparent transport it provides another means of channel estimation. This OFDM channel estimation can be performed for complimentary channel measurements or for enhancing transmission performance in frequency selective channels.

In the following the demonstrated fiber-wireless transmission experiments in the 60 GHz and 300 GHz band are outlined. 100 Gbit/s data rates are achieved in both bands via high bandwidth IF-OFDM-QAM modulation and dual-polarization transmission.

3.4.1 Experimental Results for 60 GHz Transmission

The fiber-wireless transmission experiments were first conducted in the 60 GHz band using a commercial 70 GHz Finisar PD and WR15 SBD from Virginia diodes with a maximum detector response of $\sim$ 10 GHz. A high transmit power could be achieved through a medium power amplifier and an additional WR15 variable attenuator was employed at the wireless receiver

after 1 m transmission to emulate even larger distances. The system setup for 60 GHz measurements with highlighted bandwidth limitations of the used components is shown in Fig. 3.20.

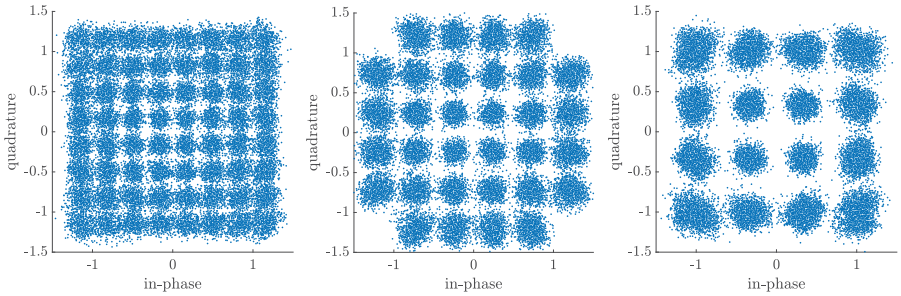

Figure 3.21
Constellation diagrams after wireless transmission at 60 GHz, envelope detection and digital demodulation of a 64 QAM signal with 4 GHz BW (a), 32 QAM with 5 GHz BW (b) and 16 QAM with 6 GHz BW (c)

Higher order modulation up to 64 QAM could be realized up to 4 GHz bandwidth with $IF = 1.5 \cdot BW$. Thereby, EVM values of −19.58 dB were demonstrated giving a gross data rate of 24 Gbit/s as shown by the constellation diagram in Fig. 3.21.a. Due to the bandwidth limitation of the used envelope detector a significant EVM increase to −18.85 dB at $BW = 5$ GHz and −17.61 dB at $BW = 6$ GHz was observed. This meant a reduction of constellation size to 32 QAM and 16 QAM – as illustrated by Fig. 3.21.b and Fig. 3.21.c respectively – was necessary, which prevented a further increase of the data rate.

In order to increase the bandwidth a heterodyne mixer receiver was employed, which has a higher IF bandwidth of 15 GHz. It furthermore does only require an IF equal to half the bandwidth because no down-conversion to baseband and thus no SSBI occurs. During the experiments with the heterodyne mixer, it was noted that a high 60 GHz LO power is necessary, which even required an amplifier after the synthesizer.

Still, a substantial signal distortion and noise floor were observed. The demodulation of the received data signals showed that the OFDM used pilots and signal processing were not sufficient for flawless carrier frequency estimation. This was caused by the free-running lasers, which induced a partially uncompensated frequency drift, which led to a substantial increase in EVM. Thus, it was barely possible to transmit 16 QAM constellations, as demonstrated by the constellation diagrams for 1 GHz bandwidth with an EVM of -11.67 dB and 10 GHz bandwidth with an EVM of -9.61 dB in Fig. 3.22.a and Fig. 3.22.b, respectively. It can be seen that similar EVM values are achieved even though the bandwidth was increased 10-fold causing a higher noise power.

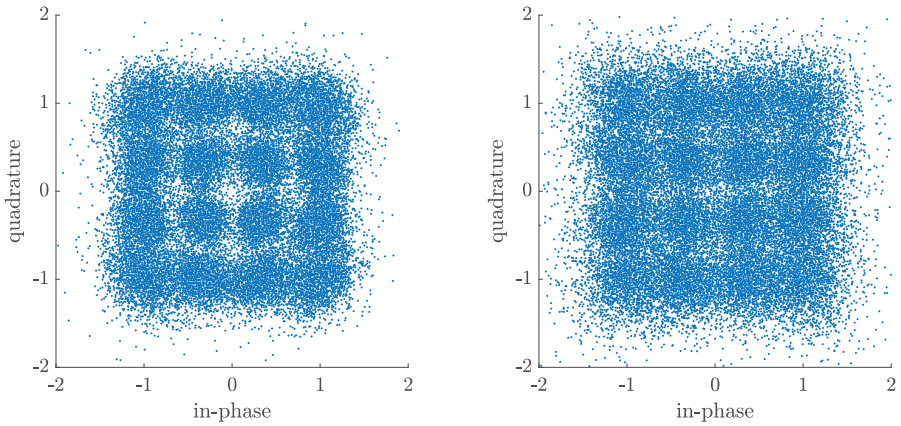

Figure 3.22
Constellation diagram of the 16 QAM signals with 1 GHz (a) and 10 GHz (b) bandwidth after wireless transmission at 60 GHz, heterodyne detection and digital demodulation

The transmission system was investigated in detail though modeling and simulations to find optimum operating conditions. Moreover, dedicated component and subsystem measurements were carried out to improve the performance. The commercial PD was replaced with a coherent photonic mixer (CPX), which provides a common-mode noise cancellation and higher output power, making the MPA at the transmitter unnecessary.

As a result, it was not only possible to improve the obtained EVM, but also to increase the usable bandwidth. This was achieved through careful adjustment of the MZM bias point and its IF drive power levels to suppress the SSBI created in the SBD below the noise floor. Thereby, the effective usable bandwidth for modulation could be doubled. Additionally, a newer WR12 SBD was employed with higher responsivity and a detector bandwidth of ~ 12 GHz.

3.4.2 Beyond 100 Gbit/s & THz Transmission Demonstration

Using an OFDM bandwidth of 12.5 GHz with 16 QAM modulation achieves a gross data rate of 50 Gbit/s. By using a guard band of only 2 GHz we were able to perform such a 50 Gbit/s transmission over our 60 GHz band link with the described bandwidth limitations.

In order to realize the projected 100 Gbit/s dual-polarization transmission was employed. Therefore, two 50 Gbit/s optical data signals were created at

orthogonal polarization states and transmitted over standard single mode fiber (SMF).

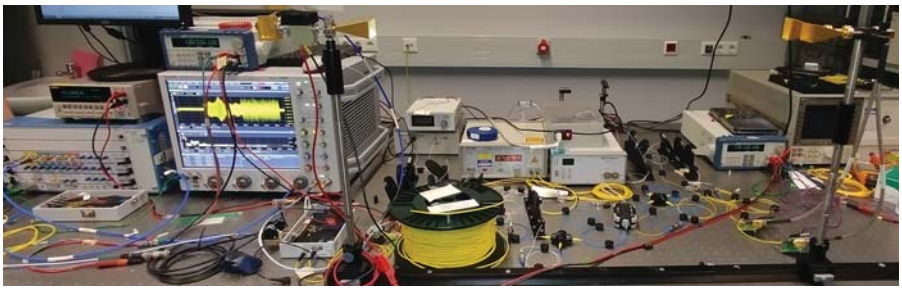

Figure 3.23
Photograph of the laboratory setup used for the 60 GHz 100 Gbit/s transmission experiments

At the radio access unit, a polarization beam splitter (PBS) was employed to divide the orthogonal polarized optical signals to two coherent photonic mixers. At each CPX an RF signal was generated by means of a polarization controlled LO and then radiated by two orthogonal polarized horn antennas in the 60 GHz band employing the laboratory setup shown in Fig. 3.23.

Dual polarization transmission is employed in the optical as well as the RF domain to effectively double the capacity of both channels. This multiplexing technique is transferred between optical and RF channel and does not degrade the link performance due to the high isolation that can be achieved. Hence, it allowed the demonstration of 100 Gbit/s throughput in the 5G designated 60 GHz channel with 14 GHz bandwidth. The employed system setup is illustrated in Fig. 3.24 with an inset showing the received IF spectrum.

The obtained transmission quality of the 100 Gbit/s 60 GHz link is illustrated in Fig. 3.25. It depicts the EVM of the transmitted subcarriers as well as the demodulated and normalized constellation diagram. When looking into the received spectrum in the inset of Fig. 3.24 a strong frequency selectivity across the transmission bandwidth is observed.

This translates to a large ± 3 dB fluctuation of the EVM per subcarrier shown in Fig. 3.25.a. This makes OFDM a good waveform candidate despite the high peak-to-average-power ratio (PAPR), as it is designed to deal with highly frequency dependent channels. As such OFDM provides efficient channel estimation and makes bit-loading feasible for further improvements of the transmitted bit rate.

The average EVM in both polarizations is -16.2 dB which results in a BER of $2.4 \cdot 10^{-3}$ (well below the $3.8 \cdot 10^{-3}$ limit for 7 % overhead HD-FEC). A bandwidth of up to 12.5 GHz has been realized, which translates to 100 Gbit/s when considering dual-polarization transmission with 16 QAM (4 bit/s/Hz).

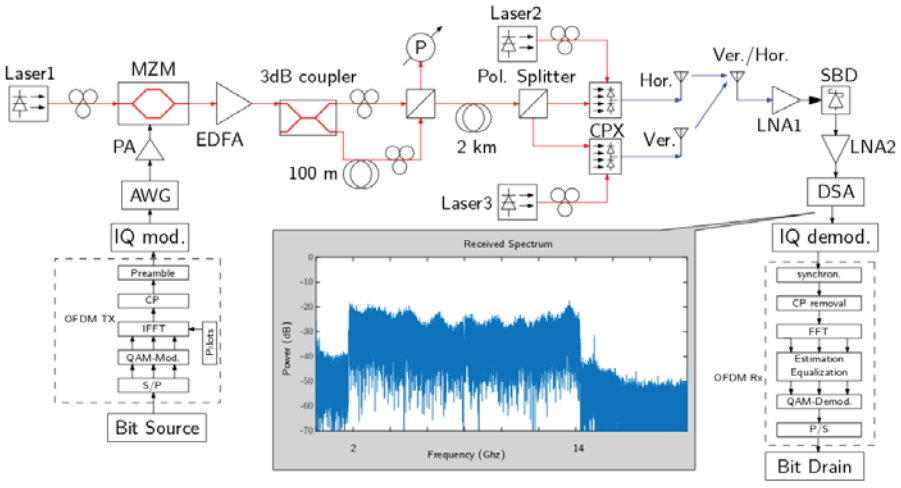

Figure 3.24
System setup for dual-polarization fiber-wireless transmission at 60 GHz

The good transmission quality is further visualized by the constellation diagram after zero-forcing in Fig. 3.25.b.

The coherent RoF approach employed in the Tera50+-project offers the capability to utilize mostly the same setup for transmission at various bands over a vast frequency range. It is only necessary to exchange the photodiode and Schottky-barrier diode for up- and down-conversion and the antennas and eventual RF amplifiers. The RF is then adjusted by tuning the LO laser and thereby the beat frequency generated by the PD.

After successful demonstrations at 60 GHz, the final step was to utilize the J-band PDs for establishing a fiber-wireless link in the 300 GHz band. A photograph of the 300 GHz link in shown in Fig. 3.26 with the Tx PD on the left side and the Rx LNA and SBD on the right side.

The main challenge when switching from 60 GHz to 300 GHz is the power limitation and high noise figure of available THz band amplifiers. Thus, the wireless link distance was limited to 20 cm, which could only be improved when using reflector or lens systems with very high directivities, that are impractical for use in real-life scenarios.

Another issue is that even the best available baseband electronics provide only a limited bandwidth – in our case up to 20 GHz – lower than the usable RF bandwidth. This meant that under the $IF = 1.5 \cdot BW$ condition only 10 GHz of bandwidth can be used for data transmission at an IF of 15 GHz. Thereby, we successfully demonstrated a 340 GHz link with 32 QAM modulation, whose transmission quality is shown in Fig. 3.27. The average EVM of the over 800 subcarrier within the 10 GHz BW depicted in Fig. 3.27.a is -17.5 dB, yielding a gross data of 50 Gbit/s at a BER of $6.9 \cdot 10^{-3}$.

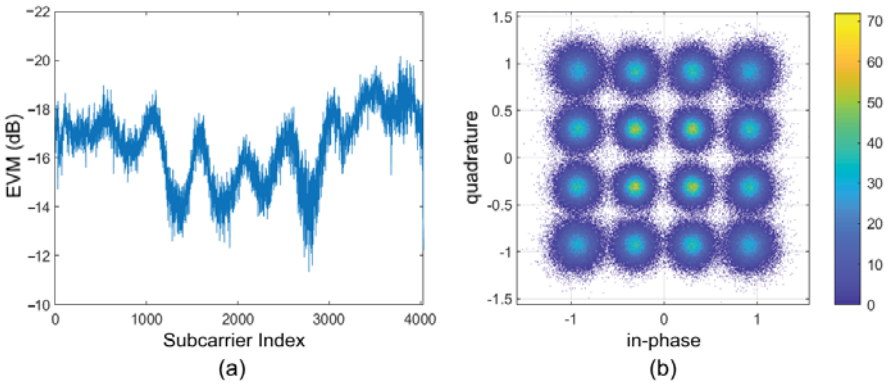

Figure 3.25
Obtained transmission quality of the polarization-duplex 12.5 GHz bandwidth 60 GHz band 16 QAM transmission displayed as the EVM per subcarrier (a) as well as the constellation diagram of the X-polarization (b). From [128] © 2020 IEEE

Using this setup even ∼ 59 Gbit/s were achieved using 64 QAM modulation with a calculated signal-to-noise-ratio of 19.42 dB as reported in [137]. This is sufficient for polarization duplex transmission of >100 Gbit/s even when considering the overhead for FEC coding.

Based on the performed investigation of the system parameters, a further increase of the OFDM bandwidth by reducing the IF is enabled. In contrast to the 60 GHz system, not the Rx SBD is the limiting factor, but the arbitrary waveform generator with its 20 GHz bandwidth. Initially, a 32 QAM signal with 20 GHz bandwidth was generated at an IF of 10 GHz, i.e. without guard band. This signal was detected at its IF via a baseband PD and received by the DSO. Thereby, the 100 Gbit/s transmission achieved an EVM of -19.21 dB, resulting in a BER of $7.42 \cdot 10^{-4}$.

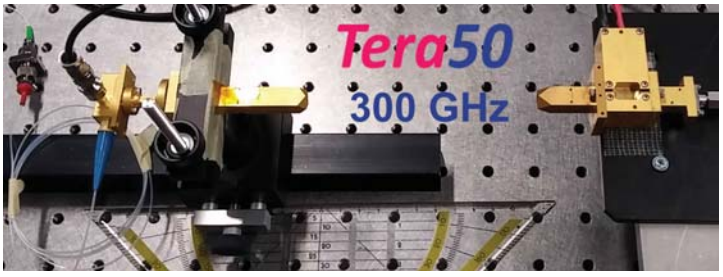

Figure 3.26
Photograph of the 300 GHz wireless link

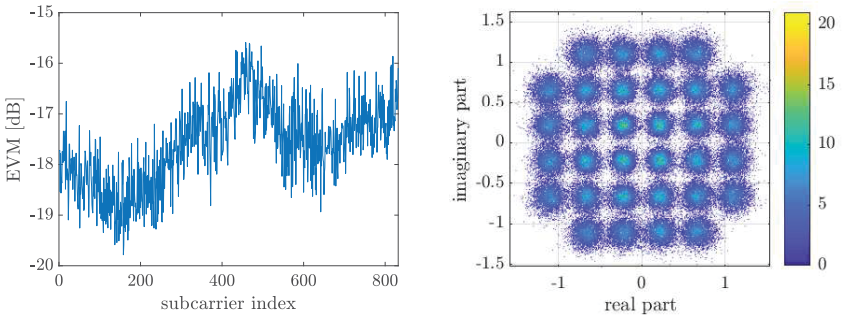

Figure 3.27
Obtained subcarrier EVM (a) and constellation diagram (b) of the 32 QAM fiber-wireless THz link with 10 GHz bandwidth at an IF of 15 GHz after 20 cm transmission at 340 GHz

For THz transmission at 340 GHz the upconversion was performed by optical heterodyning in a J-band PD from NEL and the downconversion was carried out by a WR2.8 SBD from VDI, which are also depicted in Fig. 3.26. Then, 16 QAM signals were transmitted with the PD and SBD being connected back-to-back, achieving an EVM and BER of -13.32 dB and $1.20 \cdot 10^{-2}$ at a bandwidth of 20 GHz as well as an EVM and BER of -15.16 dB and $4.81 \cdot 10^{-3}$ at a bandwidth of 16 GHz, respectively. When attaching the horn antennas for ultra-short transmission over 2 mm air distance the performance was virtually unchanged yielding an EVM and BER of -13.93 dB and $8.11 \cdot 10^{-3}$ at a bandwidth of 20 GHz as well as an EVM and BER of -14.85 dB and $3.47 \cdot 10^{-3}$ at a bandwidth of 16 GHz, of which the constellation is plotted in Fig. 3.28a.

These BERs are sufficient to allow the application of orthogonally concatenated BCH super codes, which are standardized for optical long range transmission, to get quasi-error free transmission post-FEC [138, 139]. For the 16 QAM transmission with 16 GHz bandwidth this would still amount to 56.17 Gbit/s net data rate when considering 6.7 % FEC overhead, 5 % cyclic prefix and the transmitted pilot tones.

Finally, 300 GHz band amplifiers from RPC with 25 dB gain were employed to increase the wireless distance to 20 cm and enable wireless dual-polarization transmission. Due to the high noise figure of the amplifiers of 12 dB, the signal quality degraded as illustrated in Fig. 3.28b to an EVM of -12.01 dB, yielding a BER of $2.14 \cdot 10^{-2}$ for the 16 QAM signal with 16 GHz bandwidth. Thus, LDPC (Low-density parity-check) convolutional codes with an overhead of 20% are necessary for correct signal reception [139]. Still, a 2×64 Gbit/s data rate transmission at 340 GHz carrier was demonstrated. When only considering

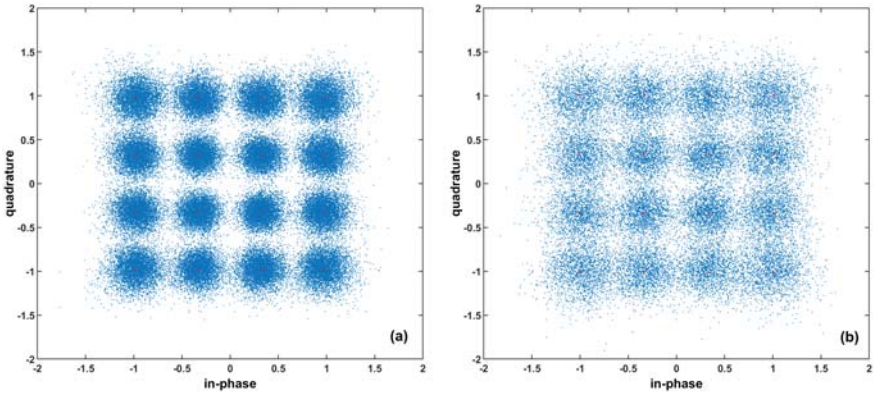

Figure 3.28
Constellation diagrams of the 16 QAM signals with 16 GHz bandwidth after 340 GHz transmission over 2 mm (a) and after dual-polarization transmission over 20 cm and subsequent 340 GHz amplification (b)

the FEC coding overhead this would still amount to 102.4 GBit/s total data rate.

3.5 Conclusion

The aim of the Tera50+-project was to develop a fiber-wireless transmission system with high bandwidth capable of 100 Gbit/s throughput. The system architecture combines coherent Radio-over-Fiber transport with photonic up-conversion via free-running lasers at the radio frontend and Schottky-barrier diode envelope detection down-conversion at the wireless receiver. Thereby, the large bandwidth of optical modulators up to 40 GHz could be exploited for high bandwidth channels, even enabling optical multiplexing for multi-channel operation.

The photonic up-conversion with an LO laser provides frequency scalability in the THz range and transparent transmission. For this application, polarization-diversity beam steering transmitters based on photonic integrated mixers and leaky-wave antennas have been fabricated for the 26 GHz 5G band. Moreover, vertical InP-based photodiodes with a 3dB-bandwidth in excess of 100 GHz have been fabricated by UDE. They provide output powers up to about −18 dBm at 300 GHz.

A channel model has been developed based on analytical descriptions as well as performed channel sounding experiments up to the THz frequency range.

Schottky-barrier diodes were exploited for frequency agnostic down-conversion, which eliminates the necessity for LOs at the wireless receiver. Furthermore, they are insensitive to phase-noise and RF carrier drift, which makes them ideal for the application with free-running lasers and allowed us to overcome limitations of often employed multiplier-chain based electronic systems. Higher order QAM modulation could still be used by exploiting IF-OFDM signals to retain phase-information in direct envelope detection.

The transmission system has been modeled in order to increase the performance through optimal bias conditions and non-linear compensation. Thereby, the projected 100 Gbit/s wireless have finally been demonstrated not only using a wide THz channel, but also within the 14 GHz spectrum available around 60 GHz for 5G applications.